

Deriving the mass distribution of M87 from globular clusters

Xiaoan Wu and Scott Tremaine

Princeton University Observatory, Peyton Hall

Princeton, NJ 08544-1001, USA

xawn@astro.princeton.edu, tremaine@astro.princeton.edu

ABSTRACT

We describe a maximum-likelihood method for determining the mass distribution in spherical stellar systems from the radial velocities of a population of discrete test particles. The method assumes a parametric form for the mass distribution and a non-parametric two-integral distribution function. We apply the method to a sample of 161 globular clusters in M87. We find that the mass within 32 kpc is $(2.4 \pm 0.6) \times 10^{12} M_{\odot}$, and the exponent of the density profile $\rho \propto r^{-\alpha}$ in the range 10 – 100 kpc is $\alpha = 1.6 \pm 0.4$. The energy distribution suggests a few kinematically distinct groups of globular clusters. The anisotropy of the globular-cluster velocity distribution cannot be determined reliably with the present data. Models fitted to an NFW potential yield similar mass estimates but cannot constrain the concentration radius r_c in the range 10 – 500 kpc.

Subject headings: Methods: statistical – galaxies: kinematics and dynamics – galaxies: fundamental parameters – galaxies: individual (M87) – galaxies: star clusters – cosmology: dark matter

1. Introduction

The mass distribution in elliptical galaxies is difficult to measure, in part because ellipticals do not contain gas or star disks like those found in spiral galaxies. The mass distribution is particularly uncertain beyond the effective radius, where the surface brightness fades rapidly. Fortunately, globular clusters (GCs) are found at large distances in many elliptical galaxies. For example, more than 8×10^3 GCs are believed to be present in M87 outside 3 times the effective radius $R_e \sim 7$ kpc (McLaughlin 1999a; Zeilinger, Møller & Stiavelli 1993). GCs in nearby galaxies provide relatively bright pointlike sources for which radial velocities can be determined. By analyzing the statistics of the positions and radial

velocities of GCs, we may constrain the mass profiles of their host galaxies and explore the dark matter distribution in the outer parts of elliptical galaxies. Planetary nebulae also provide excellent kinematic probes for similar reasons (e.g. Douglas et al. 2002).

The database of extragalactic GCs with radial velocities has been steadily growing in recent years. The most intensively observed systems are NGC 1399 (Dirsch et al. 2004) and M87. In this paper we examine the latter system. Harris (1986) and McLaughlin (1999a) observed the density profile of GCs in M87 out to 110 kpc. Mould et al. (1990) compiled a list of 43 GCs with radial velocities, from which Merritt & Tremblay (1993) derived a mass of $5 - 10 \times 10^{12} M_{\odot}$ within 50 kpc. They also estimated that about 200 and 1000 GCs would be required to derive accurately the slope of the mass profile of the galaxy and the velocity anisotropy of the GCs, respectively. Cohen and Ryzhov (1997) and Cohen (2000) obtained radial velocities for 221 GCs. This dataset was used to study the spin (Cohen and Ryzhov 1997; Cohen, Blakeslee & Ryzhov 1998; Kissler-Patig & Gebhardt 1998) and mass profile of M87 (Romanowsky & Kochanek 2001).

Although there is significant rotation in the M87 GC system, the fractional kinetic energy in rotation $(\Omega R/\sigma)^2 \sim 20\%$ is relatively small, so it should be safe to ignore rotation in our analysis and adopt the assumption that the system is spherical (Côté et al. 2001). Thus the data pairs $[R, v_z]$ contain all available dynamical information, where R is the projected distance from the GC to the center of the galaxy, and v_z is its velocity in the line of sight. To convert angular distance to physical distance, we adopt a distance to M87 of 16.3 Mpc (i.e. 79 pc arcsec⁻¹) following Cohen (2000).

Maximum likelihood analysis provides a powerful tool to analyze discrete data. It was used to derive the mass distribution of spherical galaxies first by Merritt (1993) and Merritt & Saha (1993). We describe our method for deriving spherical mass distributions from discrete data in Section 2. We use simulated data to test our method in Section 3. In Section 4 we constrain the mass profile of M87 and the distribution function (hereafter DF) of its GCs. The mass distribution of M87 has been determined from GC kinematics by several authors, including Merritt & Tremblay (1993), Cohen and Ryzhov (1997) and Romanowsky & Kochanek (2001). The study most similar to ours is that of Romanowsky & Kochanek (2001). We compare our method and results to theirs in Section 5. Section 6 contains conclusions.

2. Methods

We wish to constrain the potential $\Phi(r)$ of a spherical system from a set of discrete data pairs $[R_i, v_{zi}]$. In a spherical system, the DF depends on at most two integrals of motion, energy E and scalar angular momentum L , and thus takes the form $f(E, L)$. We normalize so that

$$\int f(E, L) d^3\mathbf{x} d^3\mathbf{v} = 1. \quad (1)$$

We introduce a Cartesian coordinate system (x, y, z) with origin at the galactic center, and z -axis along the line of sight. In this system, the projected radius is

$$R = \sqrt{x^2 + y^2}. \quad (2)$$

The probability that a given GC is found in the interval $dR dv_z$ is $2\pi R g(R, v_z) dR dv_z$, where

$$g(R, v_z) = \int f(E, L) dz dv_x dv_y. \quad (3)$$

Because of spherical symmetry, we may assume without losing any information that all GCs lie in the $x - z$ plane and $x > 0$. Thus we have

$$\begin{aligned} E &= \Phi(r) + \frac{1}{2}(v_x^2 + v_y^2 + v_z^2), \\ L &= \sqrt{(v_z R - v_x z)^2 + v_y^2 (R^2 + z^2)}, \end{aligned} \quad (4)$$

Given a potential $\Phi(r)$ and a DF $f(E, L)$, the likelihood of observing the data pairs $[R_i, v_{zi}]$ is

$$\begin{aligned} LH(\Phi, f) &\equiv LH([R_i, v_{zi}]|\Phi, f) \\ &= \prod_i g(R_i, v_{zi}|\Phi, f) \cdot 2\pi R_i \\ &\propto \prod_i g(R_i, v_{zi}|\Phi, f). \end{aligned} \quad (5)$$

The maximum likelihood method assumes that *the best estimate of the potential and DF is the one that maximizes $LH(\Phi, f)$* . More generally, Bayes' theorem states that if we know some prior information H which gives a prior probability $P(\Phi, f|H)$, we should maximize the posterior probability $P(\Phi, f|H)LH(\Phi, f)$ rather than the likelihood.

This formalism can easily be generalized to account for selection effects and observational errors in radial velocities. For example, in most surveys we observe GCs only in a limited

range of radii ($R_{s0} < R < R_{s1}$). To account for this limitation, we simply modify the normalization to require that

$$\int_{R_{s0}}^{R_{s1}} g(R, v_z) 2\pi R dR \int dv_z = 1. \quad (6)$$

To account for the errors in radial velocities, we just need to calculate LH with $g(R, v_z)$ replaced by

$$g'(R, v_z) = \frac{1}{\sqrt{2\pi}\sigma_v} \int g(R, v_z) e^{-(v - v_z)^2/2\sigma_v^2} dv. \quad (7)$$

Here we have assumed that the error σ_v is the same for all GCs, although the method is easily generalized to individual measurement errors. Note that our method also probes, though with less power, the potential beyond the maximum survey radius R_{s1} , both because we observe the projected distribution, which includes GCs with radial distances to the galactic center larger than R_{s1} , and because some GC orbits have apocenters outside R_{s1} .

In principle, all physically possible potentials and DFs should be explored to maximize $LH(\Phi, f)$. The most general way to do so is to assume non-parametric forms for both potentials and DFs, but this is cumbersome and computationally expensive. Instead we optimize within a family of parametrized potentials: we assume an analytical form $\Phi(r, \mathbf{X})$ and infer the parameters \mathbf{X} (which can be viewed as a row vector). For example, we may assume a power-law density-potential pair

$$\begin{aligned} \rho(r) &= \rho_0 \left(\frac{r}{r_0} \right)^{-\alpha}, \\ \Phi(r) &= \frac{4\pi G \rho_0 r_0^2}{(2-\alpha)(3-\alpha)} \left(\frac{r}{r_0} \right)^{2-\alpha} \quad (\alpha < 3), \end{aligned} \quad (8)$$

where r_0 is an arbitrary radius, and then $\mathbf{X} = \{\rho_0, \alpha\}$. We also investigate the Navarro, Frenk & White (1997) density-potential pair,

$$\begin{aligned} \rho(r) &= \frac{\rho_0}{\frac{r}{r_c} \left(1 + \frac{r}{r_c} \right)^2}, \\ \Phi(r) &= -4\pi G \rho_0 r_c^2 \frac{\ln \left(1 + \frac{r}{r_c} \right)}{\frac{r}{r_c}}. \end{aligned} \quad (9)$$

Here r_c is the concentration radius and $\mathbf{X} = \{\rho_0, r_c\}$.

If the DF $f(E, L)$ were known, the problem of optimizing the parameters \mathbf{X} would be easy to solve. We would calculate LH as a function of \mathbf{X} and figure out where LH peaks. However, in practice the DF is an unknown function, and we have to derive the DF and \mathbf{X} simultaneously. This can be done by parametric or non-parametric methods.

In the parametric method (Merritt & Saha 1993), we choose a limited number of basis functions $f_k(E, L)$ (i.e. a complete set of basis functions truncated to some order N), which are smooth in phase space. Thus, the DF is approximated as

$$f(E, L) = \sum_k w_k f_k(E, L), \quad k = 1, \dots, N. \quad (10)$$

This method ensures that the derived DF is smooth; however, it is difficult to ensure that $f(E, L) \geq 0$ for all (E, L) since neither w_k nor f_k is necessarily non-negative. Furthermore, if N is small we cannot ensure that equation (10) gives a good approximation to the actual DF. Of course, we can always increase N to improve the approximation, but then we cannot ensure that the best-fit DF will be smooth.

In the non-parametric method (Merritt 1993), we divide the $E - L$ space into $N_E \times N_L$ bins, which are denoted by the double index mn , $m = 1, \dots, N_E$, $n = 1, \dots, N_L$. Notice that the DF is isotropic if $N_L = 1$ and otherwise may be anisotropic. Then we construct a set of top-hat functions,

$$h_{mn}(E, L) = \begin{cases} V_{mn}^{-1} & \text{if } V_{mn} \neq 0 \text{ and } (E, L) \in \text{bin } mn \\ 0 & \text{otherwise,} \end{cases} \quad (11)$$

where $V_{mn} \equiv \int_{\text{bin } mn} d^3\mathbf{x} d^3\mathbf{v}$ is the phase-space volume within the survey limits that is associated with bin mn . Thus, we have

$$\int h_{mn}(E, L) d^3\mathbf{x} d^3\mathbf{v} = 1, \quad (12)$$

$$f(E, L) = \sum_{m,n} w_{mn} h_{mn}(E, L), \quad (13)$$

$$f_{mn} = \begin{cases} w_{mn}/V_{mn} & \text{if } V_{mn} \neq 0 \\ 0 & \text{otherwise,} \end{cases} \quad (14)$$

$$\sum_{m,n} w_{mn} = 1, \quad (15)$$

$$\mathbf{W} \equiv \{w_{mn}\}. \quad (16)$$

Here w_{mn} is simply the fraction of GCs in bin mn , f_{mn} is the phase space density of GCs in bin mn , and $f(E, L)$ and $h_{mn}(E, L)$ are normalized so that their integrals over phase space within the survey limits are unity.

In our calculation, the bin mn is defined by

$$\begin{aligned} E_{m-1} &\leq E < E_m, \\ \frac{n-1}{N_L} L_c(E_m) &\leq L < \frac{n}{N_L} L_c(E_m), \end{aligned} \quad (17)$$

where E_{m-1} and E_m are the lower and upper energy limits of the bin, and $L_c(E)$ is the maximum angular momentum at energy E , corresponding to a circular orbit. These bins cover all of the allowed region in $E - L$ space and may also cover some unallowed regions.

Each $h_{mn}(E, L)$ gives a normalized distribution in (R, v_z) space,

$$g_{mn}(R, v_z) = \int h_{mn}(E, L) dv_x dv_y dz. \quad (18)$$

Notice that $g_{mn}(R, v_z)$ depends on Φ (thus \mathbf{X}) but is independent of the DF specified by \mathbf{W} . An algorithm for evaluating $g_{mn}(R, v_z)$ efficiently is shown in Appendix A. To account for errors in radial velocities, the distribution should be convolved with a one-dimensional Gaussian function as in equation (7). We use the convolved distribution hereafter and drop the prime symbol for simplicity.

Due to the linearity of equations (3) and (13), we have

$$\begin{aligned} g(R, v_z) &= \sum_{m,n} w_{mn} g_{mn}(R, v_z), \\ LH(\mathbf{X}, \mathbf{W}) &\propto \prod_i g(R_i, v_{zi}) \\ &= \prod_i \sum_{m,n} w_{mn} g_{mn}(R_i, v_{zi}). \end{aligned} \quad (19)$$

Therefore, for a given set of observations $[R_i, v_{zi}]$, the likelihood is a function of \mathbf{X} and \mathbf{W} only. For a fixed potential specified by the parameters \mathbf{X} , we can calculate $g_{mn}(R_i, v_{zi})$, then maximize $LH(\mathbf{X}, \mathbf{W})$ with respect to \mathbf{W} . We may then vary \mathbf{X} to search for a global maximum $LH(\mathbf{X}, \mathbf{W})$.

An advantage of this method is that we need only ensure that all w_{mn} are non-negative to guarantee that $f(E, L) \geq 0$. However, this method does not generally give smooth DFs. The derived DFs look like the sum of a set of δ -functions (Merritt 1993). This is a drawback, since to some extent the irregularities in the DFs are fitting the statistical fluctuations in the data rather than the signal. In other words it is an ill-posed problem to infer $g(R_i, v_{zi})$ from a small set of data points. One way to approach this problem is to maximize a “penalized likelihood” instead, which can be defined using entropy maximization (Richstone & Tremaine 1988) or regularization (Merritt 1993; Rix et al. 1997).

By adding an entropy term, we maximize the function

$$T \equiv \ln LH + \alpha S, \quad (20)$$

$$S \equiv - \int C(f) d^3 \mathbf{x} d^3 \mathbf{v}, \quad (21)$$

where α is a parameter chosen to control the degree of smoothness of the DF, and $C(f)$ is a convex function of f such as $f \ln f$. Adding the entropy term tends to force the DF to be uniform in phase space (in the limit of large α , the data become irrelevant and the maximum value of T occurs for $f = \text{const}$). This tendency is particularly undesirable in our case because there is a large phase volume at high energy, so that large α tends to place more GCs in a high energy state. We have done simulations to test this method and found that the derived DF is either too irregular for small α or has an excess high energy tail for large α .

To implement regularization, we maximize the function

$$Q(\mathbf{X}, \mathbf{W}) \equiv \ln LH - \lambda_E \Pi_E - \lambda_L \Pi_L, \quad (22)$$

where λ_E and λ_L are positive parameters that adjust the degree of smoothness of the DF and Π_E and Π_L are dimensionless positive-definite functions of the DF. There are several natural forms for Π_E , including

$$\Pi_E = \left\langle \left(\frac{\partial \ln f}{\partial (E/E_c)} \right)^2 \right\rangle \quad \text{uniform form,} \quad (23)$$

$$\Pi_E = \left\langle \left| \frac{\partial^2 \ln f}{\partial (E/E_c)^2} \right| \right\rangle \quad \text{exponential form,} \quad (24)$$

$$\Pi_E = \left\langle \left| \frac{\partial^2 \ln f}{\partial \ln(E/E_c)^2} \right| \right\rangle \quad \text{power-law form,} \quad (25)$$

where E_c is a normalizing constant. The names indicate what functions minimize Π_E ; for example, the uniform form is zero if $f = \text{const}$, the exponential form is zero if $f \propto \exp(-\beta E)$, where β is a constant, etc. The angle brackets denote an average over area in $E - L/L_c(E)$ space; for example, if we use a fixed energy interval for all bins, the exponential form is proportional to

$$\sum_{m,n} \left| \ln f_{(m+1)n} - 2 \ln f_{mn} + \ln f_{(m-1)n} \right|, \quad (26)$$

in case no V_{mn} is zero. The term Π_L smoothing the DF along the L direction can be written similarly.

Before we choose the form of Π_E and Π_L , it is helpful to discuss the meaning of the regularization term. Equation (22) is equivalent to

$$e^Q = e^{-\lambda_E \Pi_E - \lambda_L \Pi_L} LH(\Phi, f). \quad (27)$$

Therefore, maximizing Q is equivalent to maximizing the posterior probability if the prior probability for f is

$$P(f|H_f) \equiv e^{-\lambda_E \Pi_E - \lambda_L \Pi_L}. \quad (28)$$

By choosing λ_E and Π_E , we are assuming some prior information H_f , i.e., a specific degree of smoothness and shape of the DF. Therefore, the smoothing terms assess the physical plausibility of the DF (Cox & O’Sullivan 1990).

Generally, DFs of GCs are strongly non-uniform in the sense that they may change amplitude by a few orders of magnitude over the observable range. For example, given a logarithmic potential and a GC density profile

$$\Phi = 2\sigma^2 \ln r, \quad \nu(r) \propto r^{-3}, \quad (29)$$

the corresponding isotropic DF is

$$f(E) \propto e^{-3E/2\sigma^2}. \quad (30)$$

Over the range $R_0 < R < R_1$, the DF at zero velocity will vary by a factor of $(R_1/R_0)^3$, which is about 3000, given that the ratio R_1/R_0 is 110 kpc/7 kpc ~ 15 in the case of M87 (see §4).

Given this large variation, neither entropy maximization as in equation (21) nor the uniform form of the regularization term in equation (23) is appropriate, because they tend to favor a uniform DF over the entire phase space. The exponential and power-law forms in equations (24) and (25) give more freedom and favor exponential or power-law forms for the DF, which are more physically reasonable. We adopt the exponential form throughout this paper.

For convenience, we define

$$Q_{max}(\mathbf{X}) \equiv \max_{\mathbf{W}} Q(\mathbf{W}, \mathbf{X}), \quad (31)$$

which is Q maximized with respect to the weights \mathbf{W} . The function $Q(\mathbf{W}, \mathbf{X})$ usually has a number of local maxima in \mathbf{W} at a fixed set of potential parameters \mathbf{X} . We attempt to find the global maximum in this landscape using simulated annealing and the downhill simplex

method, as discussed in Press et al. (2003). The method does not guarantee that we have found the global maximum, so we try several different initial values of \mathbf{W} and choose the largest maximum found from any of these initial conditions. The optimization process turns out to consume most of the computational resources required by this method.

We may also assume some prior information H_X for the potential parameters, which gives a prior probability $P(\mathbf{X}|H_X)$. For example, in the power-law potential (eq. 8), it is reasonable to assume a uniform prior in $(\ln \rho_0, \alpha)$, thus we have

$$P(\mathbf{X}|H_X) = \rho_0^{-1}. \quad (32)$$

Then the probability distribution of the potential parameters \mathbf{X} is

$$P(\mathbf{X}) \propto P(\mathbf{X}|H_X)e^{Q_{max}(\mathbf{X})}. \quad (33)$$

We may also incorporate the observed surface number density profile $\Sigma_{obs}(R_j)$ of the GCs and its error $\sigma_\Sigma(R_j)$ as an additional constraint in our calculation since this may be available for many more GCs, over a larger survey area than have measured velocities. We maximize the quantity

$$Q' \equiv \ln LH - \frac{\chi^2}{2} - \lambda_E \Pi_E - \lambda_L \Pi_L, \quad (34)$$

$$\chi^2 = \sum_j \frac{(\Sigma(R_j) - \Sigma_{obs}(R_j))^2}{\sigma_\Sigma(R_j)^2}, \quad (35)$$

$$\begin{aligned} \Sigma(R) &\propto \int g(R, v_z) dv_z \\ &= \sum_{m,n} w_{mn} \int g_{mn}(R, v_z) dv_z, \end{aligned} \quad (36)$$

where both $\Sigma(R)$ and $\Sigma_{obs}(R)$ should be normalized so that $2\pi \int R dR \Sigma(R)$ and $2\pi \int R dR \Sigma_{obs}(R)$ are unity within the survey limit of GC number counting.

How should we choose λ_E and λ_L ? If these parameters are set too small, they do not smooth the DF at all. If they are set too large, the DF is forced to a specific functional form that may not be demanded by the data. Notice that in contrast to many problems such as least-squares fitting (Press et al. 2003) the likelihood is only known to within a multiplicative constant, so the goodness of fit can only be assessed in a relative sense. When maximizing Q' (eq. 34), we choose smoothing parameters following Rix et al. (1997). Assume that the minimum χ^2 in equation (35) is χ_0^2 in case of no regularization. Then we increase the smoothing parameters so that the minimum χ^2 is $\chi_0^2 + n_s^2$, where n_s corresponds to

$n_s - \sigma$ error. We call these “appropriate” smoothing parameters. A degeneracy arises in choosing two smoothing parameters from one requirement. The two parameters λ_E and λ_L control smoothness in the direction of E and L , respectively and are not necessarily equal. Fortunately, we find that all “appropriate” pairs of smoothing parameters give similar results for derived potentials and energy distributions, although, not surprisingly, the derived anisotropy can be very different depending on the value of λ_L . Of course, with more data, the values of smoothing parameters will be subject to tighter constraints. Therefore, we may recover the anisotropy if enough data is available.

3. Simulations

We first test our algorithm using simulated data. We choose a DF

$$f(E, L) = \left(e^{-(E-320)^2/100} + 0.02e^{-(E-380)^2/100} \right) e^{\gamma L/L_c(E)} \quad (37)$$

in a power-law potential (eq. 8) with $r_0 = 19$ kpc and $(\rho_0, \alpha) = (1.9 \times 10^7 \text{ M}_\odot \text{ kpc}^{-3}, 1.9)$. The energy E is in units of $(100 \text{ km s}^{-1})^2$. The anisotropy parameter γ is a constant which we choose in the range from -5 (extremely radial) to 5 (extremely tangential). The DF is chosen so that the energy distribution is bimodal, to challenge the algorithm. We generate 160 kinematic data points within the projected radius range 7–32 kpc and a surface number density profile from 7000 GCs within the projected radius range 7–110 kpc (these match the properties of the sample of M87 GCs described in §4.1).

In this case, $\mathbf{X} = \{\rho_0, \alpha\}$. Figure 1 shows the contour plot for $Q_{max}(\mathbf{X})$ for three simulations with $\gamma = -5, 0$ and 5 . The appropriate smoothing parameters are $(\lambda_E, \lambda_L) = (0.015, 0.015)$ so that $n_s = 1$. The plus signs are the best-fit model which gives the maximum $Q_{max}(\mathbf{X})$ while the asterisk signs mark the input models. The contours are $n - \sigma$ levels from the peak, i.e., $e^{-n^2/2}$ of the maximum likelihood. We run 20 simulations with γ between -5 and 5 and find that the standard errors are 10% for ρ_0 and 0.2 for α . These tests show that we can recover the potential parameters from this dataset, even for extremely anisotropic DFs.

Figure 2 shows the input and derived energy distributions of the GCs, described by

$$\mathbf{U} \equiv \left\{ \sum_n w_{mn} \right\}, \quad (38)$$

i.e., the sum of the weights over all angular-momentum bins at a given energy. The derived energy distributions (dotted lines) fit the input distributions (solid lines) reasonably well for

the nearly radial ($\gamma = 5$) and isotropic ($\gamma = 0$) DFs. However, the derived DF is shifted to low energies for the nearly radial DF ($\gamma = -5$), probably because the relatively large errors (see Figure 1) in the derived potential parameters lead to a shift of zero-energy point. Nevertheless, the bimodality of the DF is successfully recovered.

To determine whether our method can recover the anisotropy of the DF from such a small data set, we define an indicator

$$I(E, L) \equiv \frac{f(E, L)}{\bar{f}(E)} \quad \text{or} \quad I_{mn} \equiv \frac{f_{mn}}{\bar{f}(E)}, \quad (39)$$

where $\bar{f}(E)$ is the DF averaged over phase space at energy E ,

$$\begin{aligned} \bar{f}(E) &\equiv \frac{\int_E^{E+\delta E} f(E, L) d^3\mathbf{x} d^3\mathbf{v}}{\int_E^{E+\delta E} d^3\mathbf{x} d^3\mathbf{v}} \\ &= \frac{\sum_n w_{mn}}{\sum_n V_{mn}}. \end{aligned} \quad (40)$$

Figure 3 shows the weighted indicator of anisotropy

$$J(L/L_c) \equiv J_n \equiv \sum_m I_{mn} U_m, \quad (41)$$

which is a constant for an isotropic DF. The solid lines show the input and the dotted lines show the derived anisotropy indicators associated with the best-fit models in Figure 1. For the isotropic ($\gamma = 0$, dotted line) and tangential ($\gamma = 5$) DFs, we recover the anisotropy correctly, but not for the radial DF ($\gamma = -5$) and some simulations with an isotropic DF ($\gamma = 0$, dashed line). Our simulations show that there is a high probability (5 out of 20 runs) of failing to recover the anisotropy correctly. Therefore, we can not get a reliable result for anisotropy from a small (~ 160 velocities) data set with these parameters.

Our simulations suggest that we can recover the dependence of the DF on energy E reasonably well with a sample of this size but we can not reliably recover the dependence of DF on angular momentum L . This is probably because the observable distribution $g(R, v_z)$ depends more strongly on how GCs are distributed in energy than angular momentum. Of course, with more data, we may constrain the anisotropy of the DF more tightly.

4. Mass distribution of M87

4.1. A uniform dataset

Surveys of GC positions and radial velocities for M87 are described in Section 1. The largest survey of GC radial velocities is given by Côté et al. (2001), who list 278 GCs.

However, they are drawn from a variety of sources. To construct a uniform sample, we use only the data in Cohen and Ryzhov (1997): these are drawn from a survey by Strom et al. (1981), which was complete only in the radius range $90''$ – $405''$. So we have the survey limits $(R_{s0}, R_{s1}) = (7, 32)$ kpc (see Figure 4). Restricting our sample to this range, we have 161 GCs, which are shown in Figure 5. The errors in radial velocities given by Cohen and Ryzhov (1997) range between 50 – 100 km s $^{-1}$; we set the errors equal to 75 km s $^{-1}$ for all GCs.

We also incorporate the surface number density profile $\Sigma_{obs}(R_j)$, which is given with estimated error $\sigma_{\Sigma}(R_j)$ in 25 bins from 7 to 110 kpc by Harris (1986) and McLaughlin (1999a), as an additional constraint in our calculation, as described in §2. Both $\Sigma(R)$ and $\Sigma_{obs}(R)$ should be normalized so that $2\pi \int R dR \Sigma(R)$ and $2\pi \int R dR \Sigma_{obs}(R)$ are unity within the radius range 7–110 kpc. Notice that we do double count some of the GCs in 7–32 kpc since they appear in both the kinematic data $[R_i, v_{zi}]$ and in the surface density distribution $\Sigma_0(R_j)$. However, this does not affect our results in a noticeable way because there are over 7000 GCs used in the calculation of the surface density distribution.

4.2. Analysis

We have described our method in §2. In constructing our models we must choose a maximum energy E_{N_E} (eq. 17) for the cluster population, or equivalently, a largest apocenter r_m such that $\Phi(r_m) = E_{N_E}$. We choose $r_m = 300$ kpc, 9 times larger than the outer survey radius $R_{s1} = 32$ kpc. If r_m is too small, we bias our results by excluding high-energy GCs that may be present within the survey radii. If r_m is too large, the numerical work will be dominated by GCs that spend only a small fraction of their orbits within the survey radii. For comparison, Harris (1986) observed GCs out to projected radius $R = 110$ kpc.

4.3. Results

4.3.1. Isotropic power-law models

Initially we assume that the DF is isotropic ($N_E = 80$, $N_L = 1$) and the mass density profile of the galaxy is a power law (eq. 8). We set the arbitrary radius r_0 in equation (8) to be 19 kpc, near the median radius of our samples, to minimize the covariance of ρ_0 and α in their bivariate probability distribution.

In this case, $\mathbf{X} = \{\rho_0, \alpha\}$. Figures 6a,b show the contour plot of $Q'_{max}(\mathbf{X})$ and the

resulting best fit to the surface number density profile. The appropriate smoothing parameters are $(\lambda_E, \lambda_L) = (0.015, 0.015)$ so that $n_s = 2$ as described in §2. We get a very tight constraint on the potential if the DF is assumed isotropic. The isotropic models give $M(32 \text{ kpc}) = (2.6 \pm 0.3) \times 10^{12} M_\odot$ and $\alpha = 1.8 \pm 0.2$. The best fit value of α is consistent with the value 1.7 found by Romanowsky & Kochanek (2001) for similar isotropic models. Figure 7 shows the derived energy distribution of the GCs. The dotted line (bottom) is the energy distribution of GCs within projected radius $R = 7 - 32 \text{ kpc}$, which is calculated from the DF associated with the best-fit model in Figure 6a. The upper dashed line is the energy distribution of all GCs with $R \geq 7 \text{ kpc}$ in the same model. The error bars are estimated from bootstrap resampling. The energy distributions suggest that there may be kinematically distinct groups of GCs in M87.

4.3.2. Anisotropic power-law models

Figures 8a and 8b show the result of fitting models with power-law potentials and anisotropic DFs ($N_E = 40$, $N_L = 5$) to both the kinematic data and the observed surface number density, using both $\lambda_E, \lambda_L = 0$ and the appropriate smoothing parameters $(\lambda_E, \lambda_L) = (0.0025, 0.60)$ so that $n_s = 2$, respectively. The contours in Figure 8a (without regularization) and Figure 8b (with appropriate smoothing parameters) are very similar, suggesting that the estimate of potential parameters of M87 is rather insensitive to smoothing parameters. The contour in Figure 8b is more irregular and the uncertainties are larger than in Figure 6a, which is expected since anisotropy gives more freedom to adjust the DF to fit the data; however, the best-fit potential parameters $(\rho_0, \alpha) = (1.9 \times 10^7 M_\odot \text{ kpc}^{-3}, 1.9)$ (plus symbol) do not change from those for isotropic models. A secondary peak, marked by the asterisk symbol, has Q' smaller by 0.2. The derived surface number density from the best-fit model in Figure 8c has a stronger tail than that derived under the assumption of isotropy (see Figure 6b). Figure 8d shows the energy distributions of GCs within projected radius $R = 7 - 32 \text{ kpc}$ (solid line) and with $R \geq 7 \text{ kpc}$ (dotted line), which are also concentrated into a few peaks. The peak at $E \simeq 440 \times (100 \text{ km s}^{-1})^2$ accounts for the strong tail in the derived surface number density profile beyond 100 kpc.

These results are based on the estimate of background stars $5.8 \pm 0.3 \text{ stars arcmin}^{-2}$ (Harris 1986). We also investigate the case of $6.1 \text{ stars arcmin}^{-2}$. We get almost the same likelihood contours and the best-fit potential parameters change by less than $1 - \sigma$; however, the amplitude of the high-energy tail is reduced by a factor of 2.

Figure 9 shows the indicators of anisotropy $I(E, L)$ and $J(L/L_c)$. The results suggest that the GCs prefer circular orbits (high angular momentum) for the best-fit model but

radial orbits (low angular momentum) at the secondary peak. To reliably determine the anisotropy of the GCs, we need to obtain more data to give a tighter constraint on mass distribution and develop a more robust formalism of choosing smoothing parameters in the future.

To estimate the probability distribution of parameters derived from the potential, we lay down points in Figure 8b with a uniform probability distribution in $(\ln \rho_0, \alpha)$, then reject or save each point according to $Q'(\mathbf{X}, \mathbf{W})$ at that point. From the saved points, we may estimate the distribution of $M(r)$, the mass enclosed within radius r , and the exponent α . Figure 10a shows the probability distribution of $M(r = 32 \text{ kpc})$, which is derived from 4×10^4 points and has been normalized to its maximum. Figure 10b shows the probability distribution of the density slope α . The data provide a fairly tight constraint on α , which is 1.6 ± 0.4 (1- σ error).

If we stack curves like that in Figure 10a for different radii, we get the mass distribution for all radii, which is shown in Figure 11a. The solid curves mark the mean and 1,2,3- σ errors. The solid line and error bars in Figure 11b show the best estimate of $M(r)$ and its standard deviation, which gives $M(32 \text{ kpc}) = (2.4 \pm 0.6) \times 10^{12} \text{ M}_\odot$, differing from that in isotropic models by less than the error bars.

Notice that the relative error is the smallest around 32 kpc, which is reasonable since it is the maximum survey radius. The mass profile can be approximately described as an analytical form,

$$M(r) = (2.3r^{1.36})_{-(55-1.9r+0.056r^2)}^{+(63-2.4r+0.071r^2)} \times 10^{10} \text{ M}_\odot, \quad 15 \text{ kpc} < r < 110 \text{ kpc}, \quad (42)$$

where r is in units of kpc.

Also shown in Figure 11b are previously published models. The data for X-ray observations (Nulsen & Böhringer 1995) were obtained by assuming a distance of 20 Mpc to M87. The long dashed lines show their derived lower and higher limits scaled by a factor of 0.815 since we assume a distance of 16.3 Mpc. Our mass estimate is consistent with the X-ray observations in the range where they overlap. Our result is also consistent with X-ray observation by Matsushita et al. (2002) within 20% from 15 to 80 kpc by reading numbers from the double β model fit in their Figure 21. The estimate by McLaughlin (1999b) is based on X-ray observations and an assumption of a NFW dark matter halo of the Virgo cluster. The estimates by Merritt (1993) and Cohen and Ryzhov (1997) are based on the assumption of an isotropic DF.

Figure 12 shows the derived velocity dispersion profile (dotted line)

$$\sigma_z(R) = \langle v_z^2 \rangle^{1/2} = \left(\frac{\int v_z^2 g(R, v_z) dv_z}{\int g(R, v_z) dv_z} \right)^{1/2}, \quad (43)$$

which is consistent with the observed velocity dispersion profile (solid line with error bars).

4.3.3. Other models

We also investigate models with two other potentials, (i) a NFW profile (eq. 9), (ii) the potential generated by the stars, assuming constant mass-to-light ratio. We adopt the B-band luminosity profile in McLaughlin (1999b), which is smaller than the luminosity profile in Romanowsky & Kochanek (2001) by 23%, probably due to a systematic shift between different data they use.

The dotted line in Figure 11b shows the estimate for $M(r)$ for anisotropic NFW models, which is almost the same as that for power-law models beyond 20 kpc. The errors are comparable to those for power-law models. We explore NFW models with the concentration radius r_c ranging from 10 to 500 kpc. If the DF is assumed isotropic, we get $r_c = 26_{-4}^{+27}$ kpc, while models with $r_c = 100$ and 500 kpc are ruled out at 2 and $3 - \sigma$ level, respectively. However, the best-fit anisotropic NFW models with $10 \text{ kpc} < r_c < 500 \text{ kpc}$ give Q'_{max} within $2 - \sigma$, i.e., a wide range of r_c can fit the data pretty well. The models NFW1, NFW2 and NFW3 of Romanowsky & Kochanek (2001) are within $1-\sigma$ relative to our own best fit.

The constant mass-to-light ratio model gives $(M/L)_B = 125 \pm 10 \text{ M}_\odot/\text{L}_\odot$, which is much larger than the value $43 \pm 3 \text{ M}_\odot/\text{L}_\odot$ obtained by Romanowsky & Kochanek (2001) fitting the globular cluster kinematics. The difference in the B-band luminosity profiles can not account for the large gap. For the same regularization level, the maximum penalized likelihood for the best-fit powerlaw and NFW models differ by less than $1-\sigma$ while the maximum for constant M/L is smaller by 7, i.e., the constant M/L model is about $4-\sigma$ worse than for the NFW or power-law models.

5. Discussion

The mass distribution of M87 from GCs has been studied by Merritt & Tremblay (1993); Cohen and Ryzhov (1997); Romanowsky & Kochanek (2001). In general our results are consistent with the conclusions of these earlier papers. Our results are more robust than those by Merritt & Tremblay (1993) and Cohen and Ryzhov (1997) since we assume a two-integral DF rather than an isotropic DF. In some aspects, our analysis is less powerful than that of Romanowsky & Kochanek (2001), because we do not use the stellar part to constrain the mass distribution of M87. Therefore, it is not surprising that we constrain the mass distribution around the effective radius ($R_e = 7 \text{ kpc}$) rather poorly (see Figure 11). As to

the analysis of GC kinematics, our methods and results differ from those in Romanowsky & Kochanek (2001) in the following aspects.

1. Romanowsky & Kochanek (2001) fit their kinematic data to predictions for the probability distribution of radial velocities at given radii, rather than to the joint probability distribution of radius and velocity as we do. This difference in approaches is necessary because they use an incomplete sample of GCs, whereas ours is complete for $R \in (R_{s0}, R_{s1}) = (7, 32)$ kpc. Our approach is statistically more powerful but requires us to use a subset of the GCs with measured radial velocities.
2. We use regularization rather than entropy to smooth our results. As we have argued in §2, entropy smoothing tends to favor high-energy orbits. Romanowsky & Kochanek (2001) use entropy only as a numerical device to accelerate convergence to a final solution, eventually reducing the entropy contribution to a negligible value by reducing the constant α in equation (20) to a very small value. Nevertheless, this process may still tend to bias the solution towards high-energy orbits.
3. Although Romanowsky & Kochanek (2001) explore both the best fit and the uncertainties in their mass models, they do not rigorously explore the range of DFs and velocity anisotropies that are consistent with the data. We find that either radial or tangential anisotropy in the DF are allowed by the data. We also explore a wider range of mass models.

The observations of metallicity of GCs show that there are metal-rich and metal-poor globular cluster samples in M87. The metal-rich sample is more concentrated to the center (Côté et al. 2001). We tried to divide all GCs into two samples to study their kinematics individually. Ideally it would be interesting to see how the subsamples contribute to the peaks observed in the energy distribution in Figure 7 and 8d. However, the present data set is too small so that the statistics is too poor to reach a conclusion.

An important question is whether the mass distribution we have measured is a dark halo associated with M87 or with the Virgo cluster as whole. If the DF is isotropic, we find that $r_c = 26^{+27}_{-4}$ kpc, which implies that the halo is small enough that it must be associated with M87. However, for general DFs all halos with $10 < r_c < 500$ kpc fit the data, so we cannot determine whether the halo is associated with the galaxy or its host cluster.

6. Conclusions

We have investigated how to determine the mass distribution of a spherical stellar system from the kinematics of a discrete set of test particles. We use a non-parametric form for the DF, which includes the isotropic DF as a special case, and parametrized forms for the potential, and find the best-fit potential and DF using a penalized maximum likelihood method. Our method allows for selection effects, observational and statistical errors, and anisotropy in the DF. We find that the potential parameters are determined more securely than the energy distribution, which is in turn more accurate than the angular-momentum distribution. Our simulations show that mass distributions depending on two parameters can be derived rather accurately from a small number (≤ 200) of data pairs $[R_i, v_{zi}]$ and surface number density profile. Plausible estimates of the energy distribution of the test particles can also be recovered; however, we can not tell whether the DFs are isotropic or not from such a small dataset.

We have applied our method to a sample of 161 GCs between 7 kpc and 32 kpc in M87. Under the assumption that the system is spherical and the DF is isotropic, we infer that the mass of M87 within 32 kpc is $2.6 \pm 0.3 \times 10^{12} M_\odot$. The power-law index for the density profile, $\rho \propto r^{-\alpha}$ is $\alpha = 1.8 \pm 0.2$. The energy distribution suggests a few kinematically distinct groups of globular clusters. If we allow an anisotropic DF, the mass of M87 within 32 kpc is $(2.4 \pm 0.6) \times 10^{12} M_\odot$ and the power-law index is 1.6 ± 0.4 , within 1 standard deviation of the results for an isotropic DF. Anisotropic models fitted to an NFW potential yield similar mass estimates but cannot constrain the concentration radius r_c in the range 10 – 500 kpc although r_c is as small as 26_{-4}^{+27} kpc in isotropic NFW models. Assuming a constant mass-to-light ratio, the derived M/L in the B-band is $125 \pm 10 M_\odot/L_\odot$, but the model fit is substantially worse than for other mass models, and the derived mass-to-light ratio is far larger than any plausible stellar population. Our methods and results are more rigorous than earlier attempts to measure the mass of M87 from GC kinematics (Merritt & Tremblay 1993; Cohen and Ryzhov 1997) and differ from those in Romanowsky & Kochanek (2001) as discussed in §5.

We find that our mass estimates are insensitive to the smoothing parameters. Smoothing has stronger effects on the DF, which is determined less reliably. The energy distribution has multiple peaks for the chosen smoothing parameters, perhaps suggesting a few kinematically distinct groups of GCs in M87. The derived anisotropy of the GCs can not be determined at this stage. With more data, it may be possible to measure the anisotropy of the velocity distribution and to test models of GC evolution predicting that GCs on less-eccentric orbits are more likely to survive (e.g. Gnedin & Ostriker 1997).

A more statistically robust method of choosing smoothing parameters, more kinematic

data and a more accurate surface number density, especially beyond 110 kpc are the most important theoretical and observational advances needed to determine the mass distribution in M87 more accurately by this method. For example, the ongoing ACS Virgo cluster survey (Côté et al. 2004) will observe 20,000 globular clusters in the Virgo cluster, which may allow us to put tighter constraints on the mass density profiles of M87 and other member galaxies.

We thank Judy Cohen for providing the data in Figures 4 and 5 in tabular form, Michael Strauss, David Spergel, James Gunn and Robert Lupton for valuable discussions, and the referee for suggestions that significantly improved the paper. This research was supported in part by NASA grant NNG04GL47G and used computational facilities supported by NSF grant AST-0216105.

A. Calculation of $g_{mn}(R, v_z)$

We divide $E - L$ space into $N_E \times N_L$ rectangular bins. Assume that the bin mn is defined by

$$\begin{aligned} E &\in [E_{m-1}, E_m], \\ L &\in [L_{n-1}, L_n]. \end{aligned} \tag{A1}$$

We wish to determine the normalized distribution $g_{mn}(R, v_z)$ in projected radius and radial velocity corresponding to a uniform phase-space density in bin mn (eq. 18). For an anisotropic DF, this requires a three-dimensional integration over v_x , v_y and z , which is computationally expensive. We may achieve considerable speedup by integrating analytically over v_y (recall from eq. 4 that we assume that each GC lies on the x -axis). We have two constraints on v_y from inequalities (A1). Based on equation (4), we have

$$\begin{aligned} v_y^2 &\in [A, B] \\ &\equiv [2(E_{m-1} - \Phi(r)) - (v_x^2 + v_z^2), 2(E_m - \Phi(r)) - (v_x^2 + v_z^2)], \end{aligned} \tag{A2}$$

$$\begin{aligned} v_y^2 &\in [C, D] \\ &\equiv \left[\frac{L_{n-1}^2 - (v_z R - v_x z)^2}{(R^2 + z^2)}, \frac{L_n^2 - (v_z R - v_x z)^2}{(R^2 + z^2)} \right]. \end{aligned} \tag{A3}$$

Then we may set

$$I \equiv \max(\min(B, D), 0) \quad J \equiv \max(\max(A, C), 0), \tag{A4}$$

so that we have

$$\int dv_y = \max((\sqrt{J} - \sqrt{I}), 0). \quad (\text{A5})$$

This algorithm speeds up the integration by a factor of 20 or so.

REFERENCES

- Côté, P. et al., 2001, ApJ, 559, 828
- Côté, P. et al., 2004, ApJ, 153, 223
- Cohen, J. G., 2000, AJ, 119, 162
- Cohen, J. G., & Ryzhov, A., 1997, ApJ, 486, 230
- Cohen, J. G., Blakeslee, J. P., & Ryzhov, A., 1998, ApJ, 496, 808
- Cox D. D., & O’Sullivan, F., 1990, Annals of Statistics, 18, 1676
- Dejonghe, H., & Merritt, D., 1992, ApJ, 391, 531
- Dirsch, B. et al., 2004, AJ, 127, 2114
- Douglas, N. G. et al., 2002, PASP, 114, 1234
- Gerhard, O., Jeske, G., Saglia, R. P., & Bender, R., 1998, MNRAS, 295, 197
- Gnedin, O. Y. & Ostriker, J. P., 1997, ApJ, 474, 223
- Harris W. E., 1986, AJ, 91, 4
- Kissler-Patig, M., & Gebhardt, K., 1998, AJ, 116, 2237
- Matsushita, K., Belsole, E., Finoguenov, A., Böhringer, H., 2002, A&A, 386, 77
- McLaughlin, D. E., 1999a, AJ, 117, 2398
- McLaughlin, D. E., 1999b, ApJ, 512, L9
- Merritt, D., 1993, ApJ, 413, 79
- Merritt, D., 1996, AJ, 112, 3
- Merritt, D., & Saha, P., 1993, ApJ, 409, 75

- Merritt, D., & Tremblay, B., 1993, AJ, 106, 2229
- Mould, J. R., Oke, J. B., De Zeeuw, P. T., & Nemec, J. M. 1990, AJ, 99, 1823
- Navarro, J. F., Frenk, C. S., & White, Simon D. M., 1997, ApJ, 490, 493
- Nulsen, P. E. J., & Böhringer, H., 1995, MNRAS, 274, 1093
- Press, W. H., Flannery, B. P., Teukolsky, S. A., & Vetterling, W. T., 2003, Numerical Recipes in Fortran (Cambridge: Cambridge Univ. Press)
- Richstone, D. O., & Tremaine, S., 1988, ApJ, 327, 82
- Rix, H. et al., 1997, ApJ, 488, 702
- Romanowsky, A. J., & Kochanek, C. S., 2001, ApJ, 553, 722
- Strom, S. E., Forte, J., Harris, W., Strom, K. M., Wells, D., & Smith, M. 1981, ApJ, 245, 416
- Zeilinger, W. W., Møller, P., & Stiavelli, M. 1993, MNRAS, 261, 175

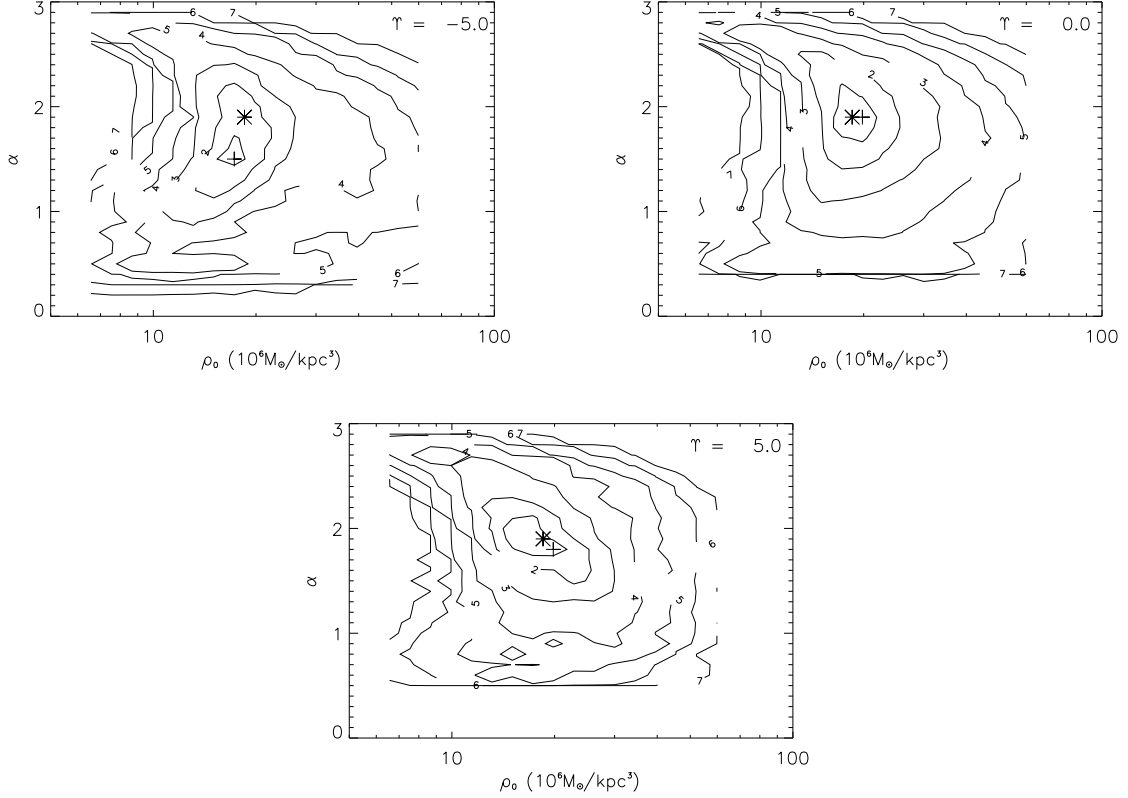


Fig. 1.— Tests of the recovery of the potential parameters $\mathbf{X} = \{\rho_0, \alpha\}$ and the DFs, using 160 data points with radial velocities and 7000 data points to define the surface density profile in a power-law potential (eq. 8). The input parameters are marked by the asterisk signs. The input DFs are described by equation (37) with anisotropy parameter $\gamma = -5$ (radial), 0 (isotropic) and 5 (tangential). Equation (24) is used for regularization. The plus signs mark the best-fit model, which gives the maximum $Q'_{max}(\mathbf{X})$ (eq. 34). The contours are $n - \sigma$ away from the peak. The tests show that we recover the potential parameters pretty well even for extremely anisotropic DF.

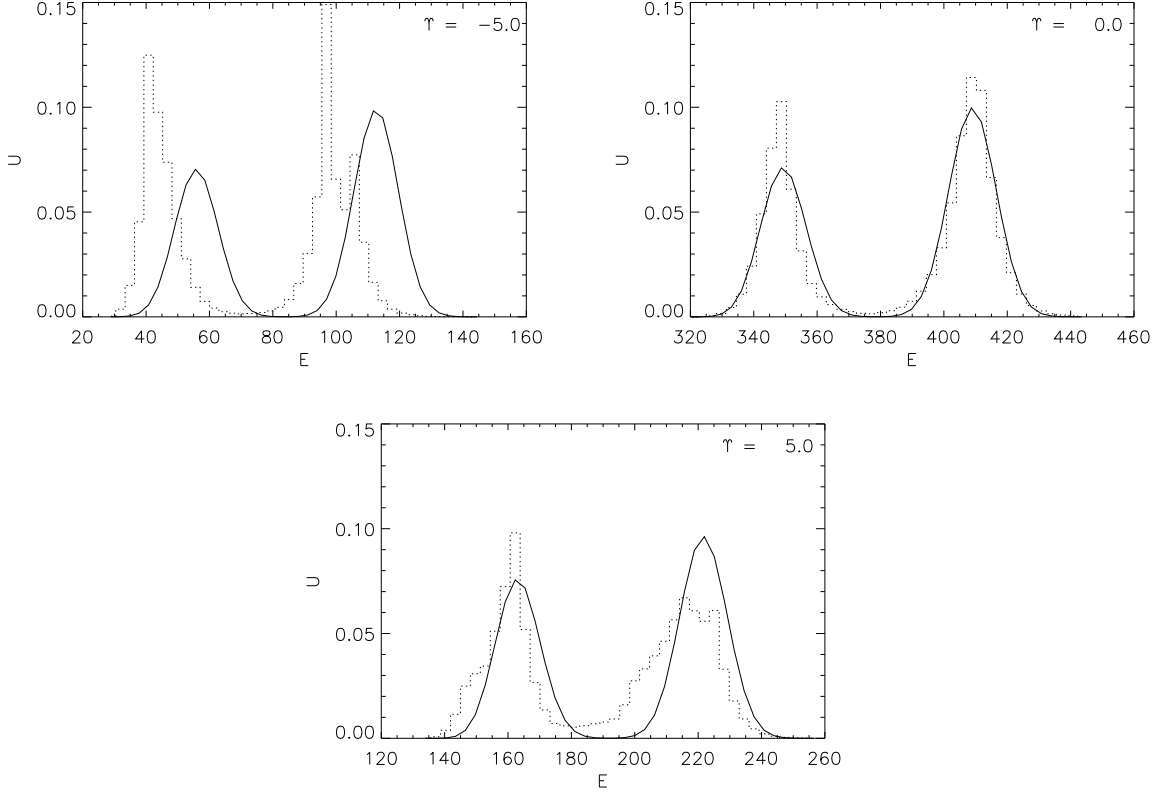


Fig. 2.— Derived energy distributions associated with the best-fit models in Figure 1. The derived energy distributions (dotted lines) successfully recover the bimodality of the input energy distributions (solid lines) for all cases. The shift between the input and derived energy distributions for the radial DF ($\gamma = -5$) is related to the relatively large errors in derived potential parameters, which shift the zero-energy point. The results show that we can recover the energy distribution from a small (~ 160 velocities) data set reasonably well.

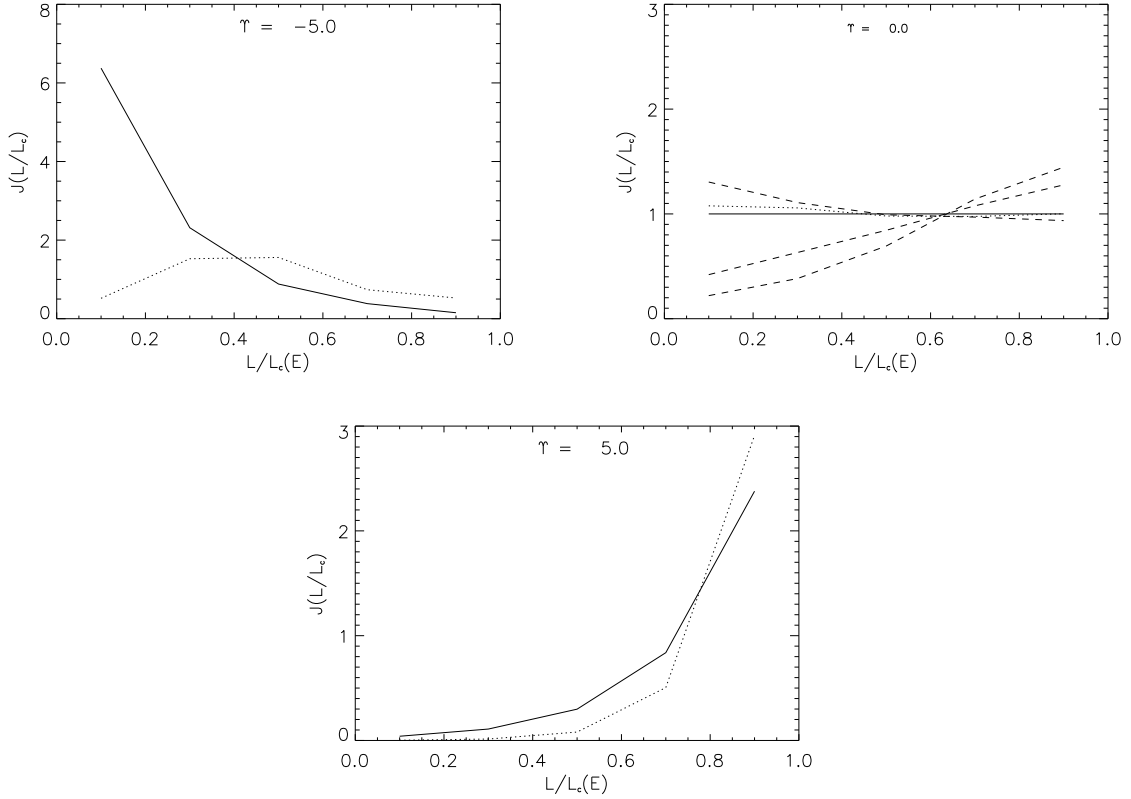


Fig. 3.— Indicators of anisotropy $J(L/L_c)$ (eq. 41). The solid lines show the input and the dotted lines show the derived anisotropy indicators associated with the best-fit models in Figure 1. For the tangential ($\gamma = 5$) DF, we recover the anisotropy correctly, but not for the radial DF ($\gamma = -5$). Some simulations with an isotropic DF ($\gamma = 0$, dashed lines) also fail to recover the correct anisotropy. Therefore, we can not get a reliable result for anisotropy from a data set of this kind.

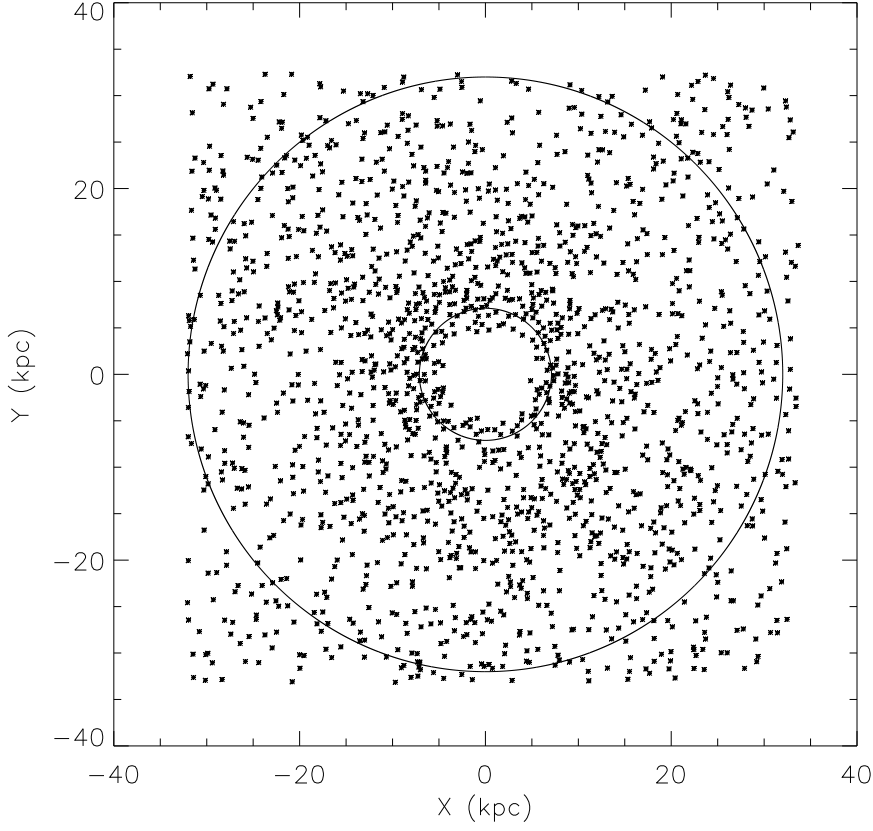


Fig. 4.— Spatial distribution of GC candidates in Cohen and Ryzhov (1997), which are taken from the photometric survey by Strom et al. (1981). To eliminate selection effects, we only use data between the two circles, which are $90''$ – $405''$ or 7–32 kpc from the center, where the Strom et al. survey was complete.

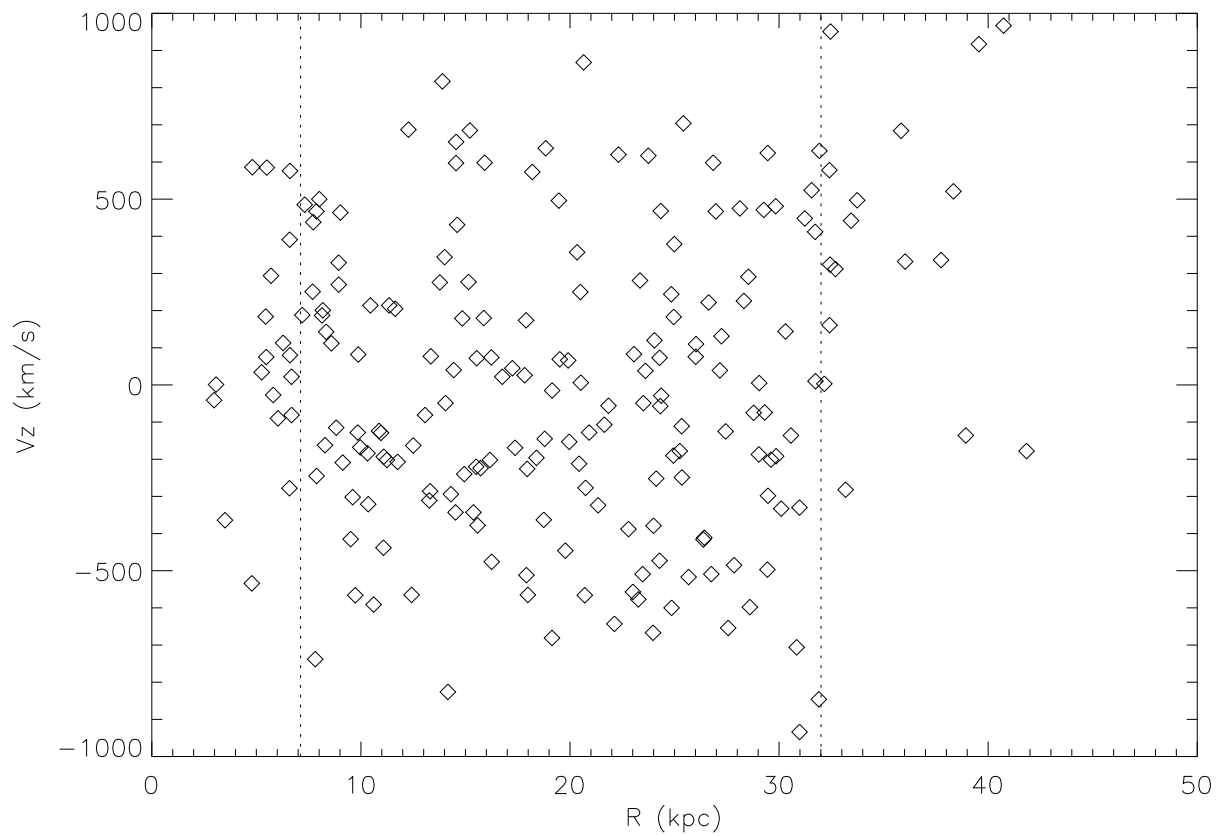


Fig. 5.— The data pairs $[R_i, v_{zi}]$ from Cohen and Ryzhov (1997) that we use to construct a uniform dataset. The data outside the survey radii (dotted lines) are excluded.

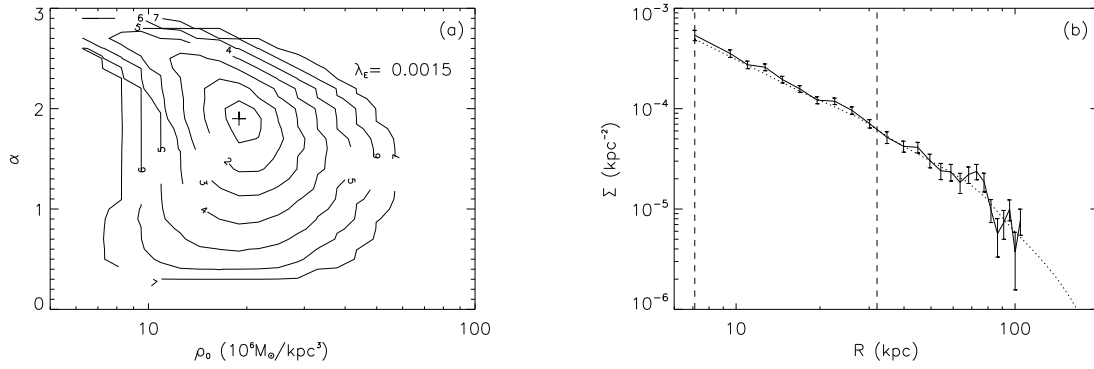


Fig. 6.— Fitting the kinematic data $[R_i, v_{zi}]$ and the observed surface number density $\Sigma_{obs}(R)$ of GCs in M87 to a power-law potential, assuming an isotropic DF. (a) Contour plot of $Q'_{max}(\mathbf{X})$ as a function of $\mathbf{X} = \{\rho_0, \alpha\}$. (b) The derived surface number density (dotted line) from maximizing $Q'(\mathbf{X}, \mathbf{W})$, compared to the observed $\Sigma_0(R)$ (solid line). The surface densities are normalized so that the total number within the range 7–110 kpc is unity. The kinematic survey limits are marked by dashed lines.

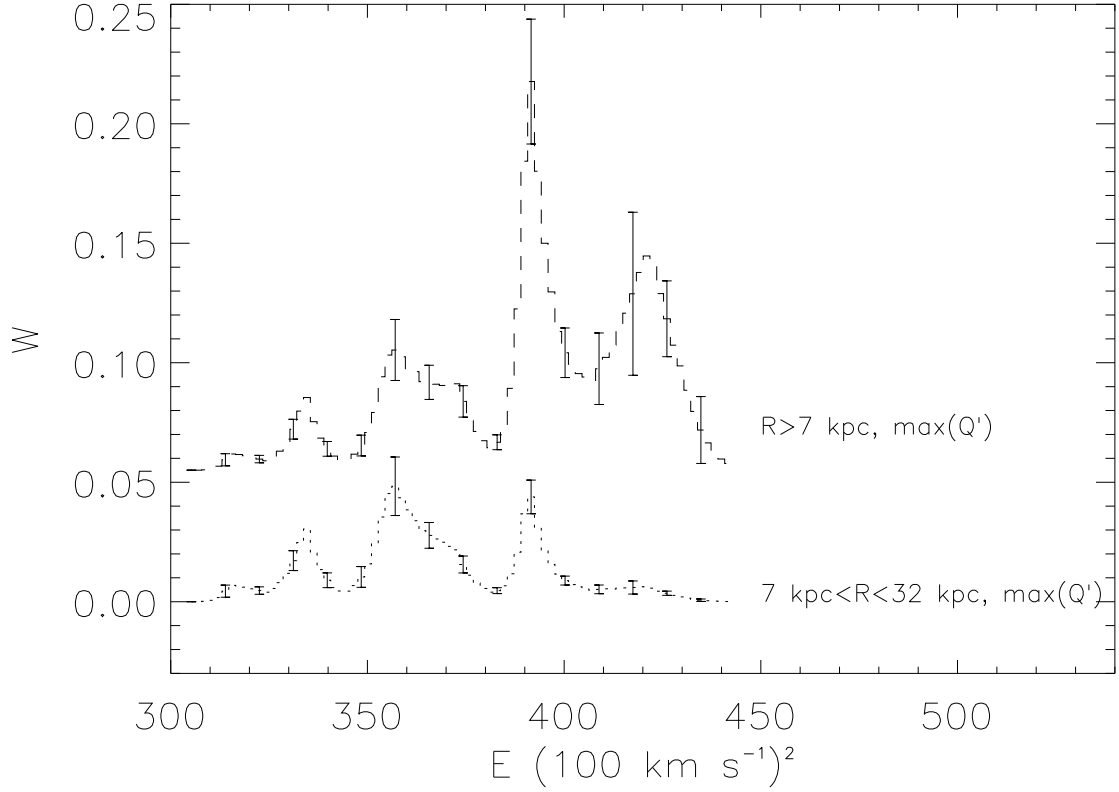


Fig. 7.— Energy distribution with the isotropic assumption: the energy weights \mathbf{W} as determined by fitting both the kinematic data and the surface density profile, as in Figure 6. The bottom dotted line refers to the energy distribution of GCs within projected radius $R = 7 - 32$ kpc and the upper dashed line to all GCs with $R \geq 7$ kpc. The error bars are estimated from bootstrap resampling.

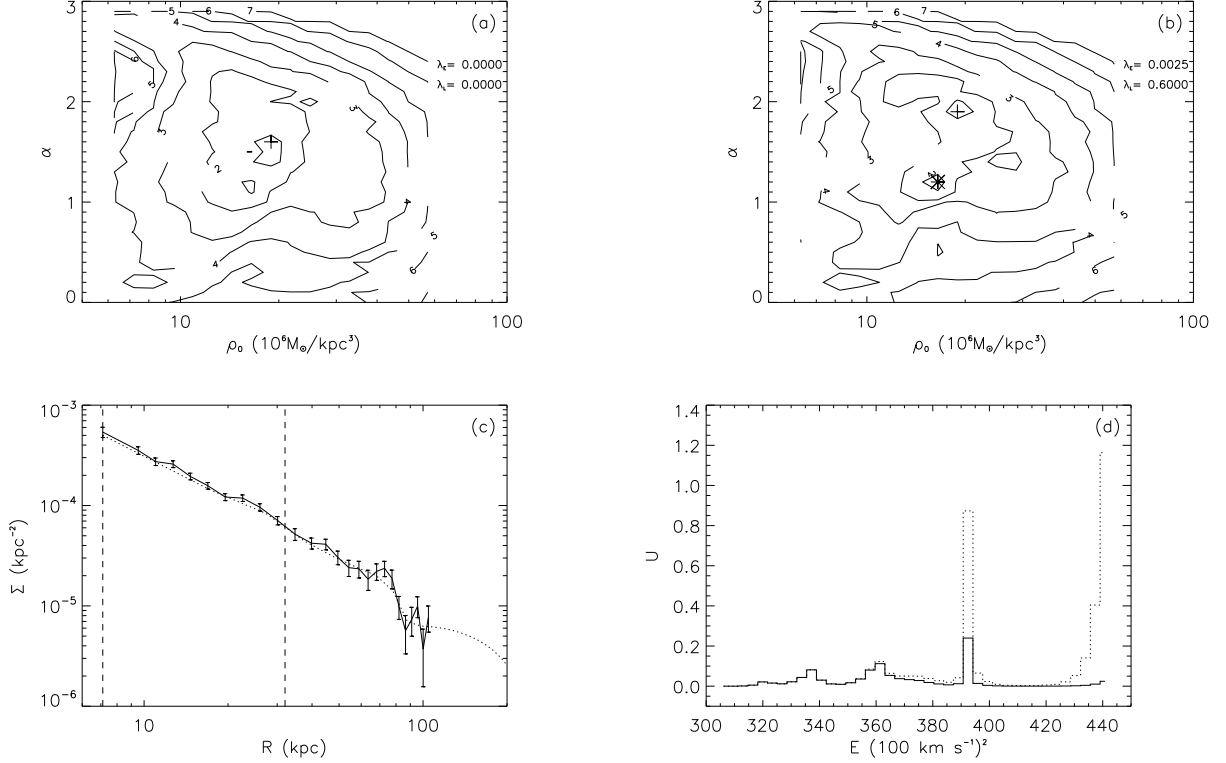


Fig. 8.— Fitting the kinematic data $[R_i, v_{zi}]$ and the observed surface number density $\Sigma_{obs}(R)$ to a power-law potential without assuming isotropy of the DF. (a) The same as Figure 6a except for anisotropic models without regularization. (b) The same as Figure 8a except for anisotropic models with appropriate smoothing parameters. The plus and asterisk mark the best-fit model and a secondary peak, respectively. (c) The same as Figure 6b except for the best-fit anisotropic model with appropriate smoothing parameters. (d) Energy distribution of GCs within projected radius $R = 7 - 32$ kpc (solid line) and with $R \geq 7$ kpc (dotted line).

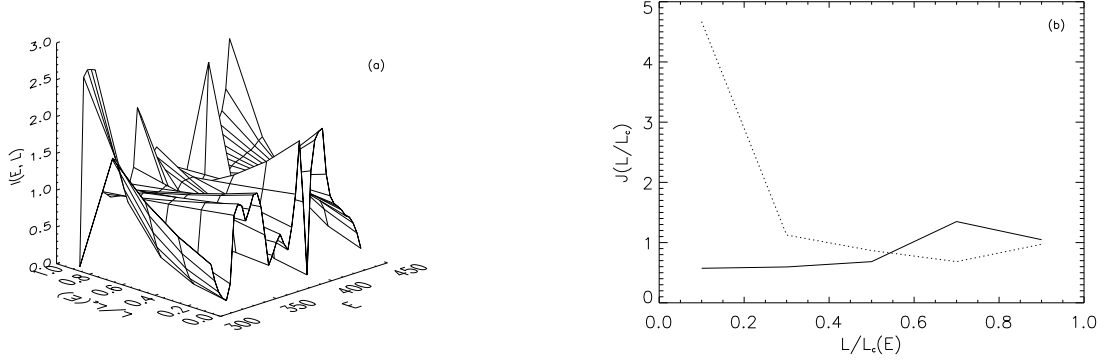


Fig. 9.— Indicators of anisotropy for $\lambda_E, \lambda_L = 0.005$. (a) $I(E, L)$ (eq. 39). (b) $J(L/L_c)$ (eq. 41) for the best-fit model (solid line) and at the secondary peak (dotted line) in Figure 8b. The behavior of the indicators suggests that the GCs may either prefer circular orbits (high angular momentum) or radial orbits (low angular momentum), depending on the mass distribution model of the galaxy.

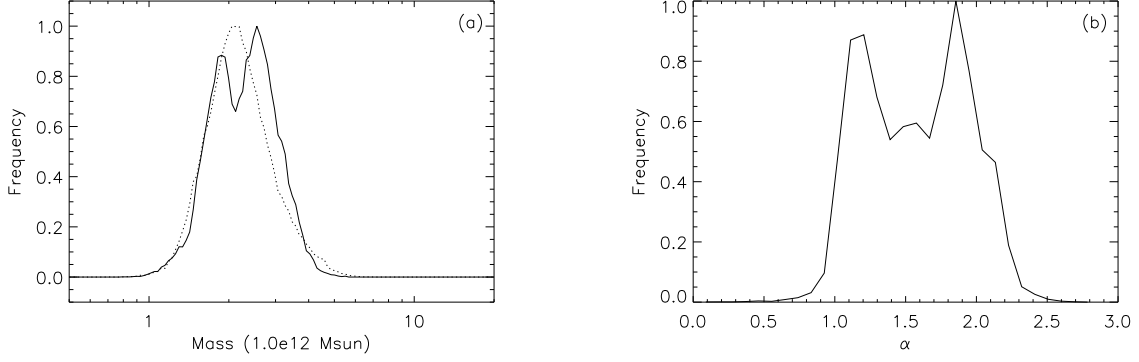


Fig. 10.— Distribution of $M(r = 32 \text{ kpc})$ and α for likelihood distribution of Figure 8b. (a) The probability distribution of $M(r = 32 \text{ kpc})$ for the power-law (solid line) and NFW models (dotted line). (b) Probability function of α for the power-law models. It gives $\alpha = 1.6 \pm 0.4$.

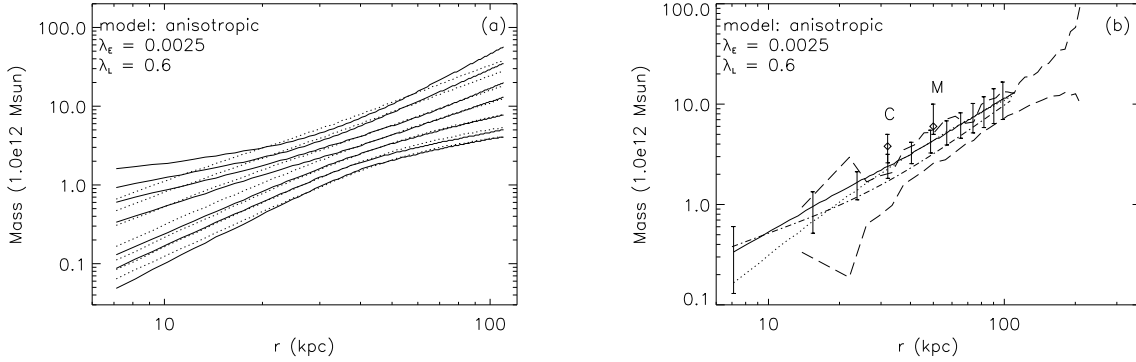


Fig. 11.— Estimates of $M(r)$, derived from Monte Carlo points laid down on Figure 8b. (a) The probability distribution of $M(r)$. The lines show the median and 1,2,3- σ errors which enclose the regions with the cumulative probabilities of 68.3%, 95.4%, 99.7% for the power-law models (solid lines) and the NFW models (dotted lines). (b) The solid and dotted lines show the estimates for $M(r)$ by assuming power-law and NFW density profiles, respectively. The error bars indicate the uncertainties in the mass estimates, which are similar for both models. The other models are: Merritt & Tremblay (1993) (marked by “M”), Cohen and Ryzhov (1997) (marked by “C”), upper and lower limits from X-ray observation by Nulsen & Böhringer (1995) (long dashed lines), McLaughlin (1999b) (dot-dashed line). The best-fit model NFW2 (star+halo) in Romanowsky & Kochanek (2001) is within 5% of our best-fit power-law model from 7 kpc to 110 kpc, thus is not shown for clarity. However, considering the large error bars ($> 30\%$) in our models, it is probably a coincidence that the two results are so close. Our result is also consistent with X-ray observation by Matsushita et al. (2002) within 20% from 15 to 80 kpc by reading numbers from the double β model fit in their Figure 21.

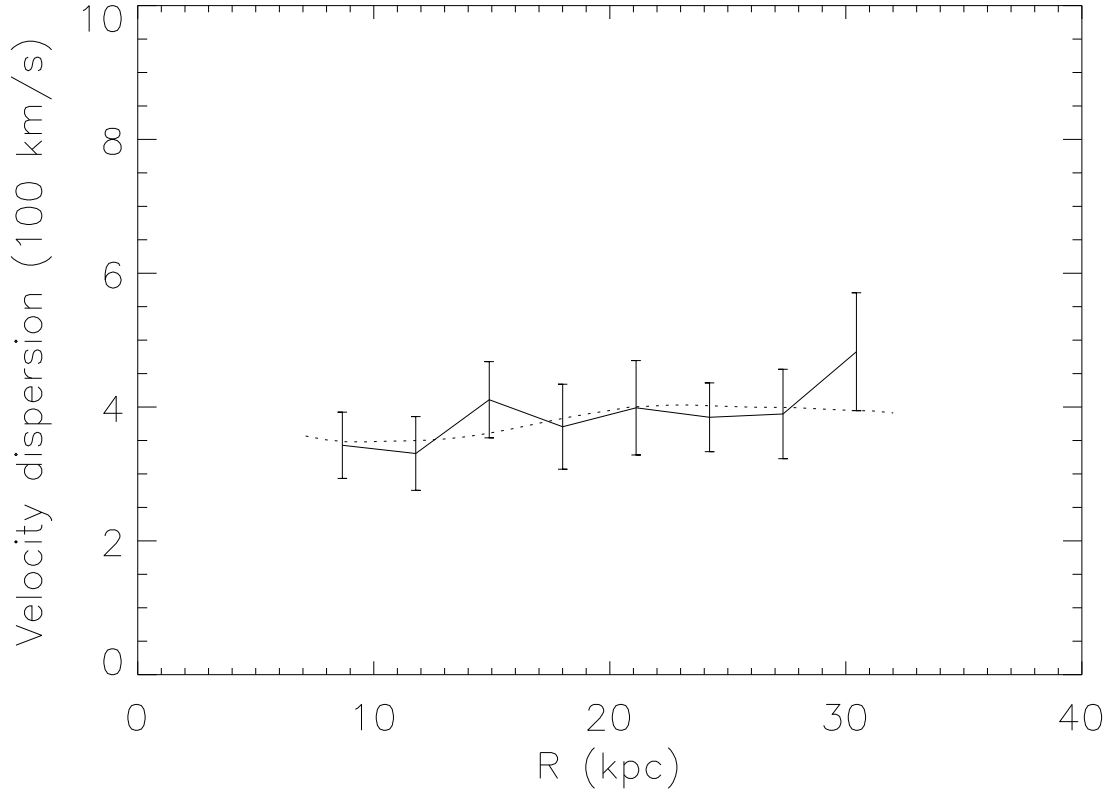


Fig. 12.— Velocity dispersion, including assumed observational errors of 75 km s^{-1} in the theoretical model. The dotted line is derived from the best-fit anisotropic power-law model, which is consistent with the observations (solid line with error bars).